iScience

CellPress

Article

Natrium Doping Pushes the Efficiency of Carbon-Based $CsPbI_3$ Perovskite Solar Cells to 10.7%

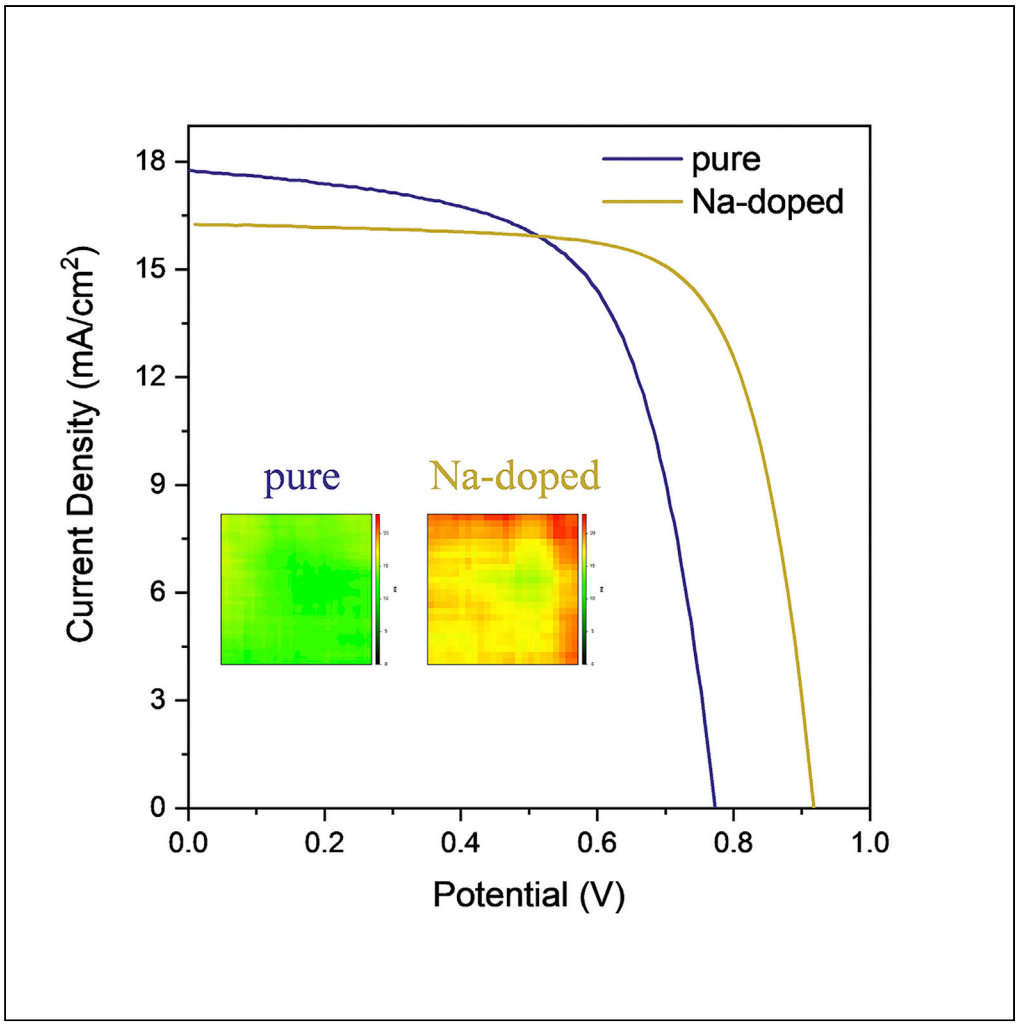

Sisi Xiang, Weiping Li, Ya Wei, ..., Liqun Zhu, Shihe Yang, Haining Chen

chsyang@ust.hk (S.Y.)
chenhaining@buaa.edu.cn (H.C.)

HIGHLIGHTS

Na doping improves the morphology and enhances the crystalline quality of $CsPbI_3$ film

All energy band levels of $Cs_{0.95}Na_{0.05}PbI_3$ are lifted up to match contact electrodes

Na-doped C-PSC achieves a PCE of 10.7%, a record value of the $CsPbI_3$ PSC without HTM

The non-encapsulated Na-doped C-PSCs exhibit excellent stability in air

Xiang et al., iScience *15*, 156–164
May 31, 2019
https://doi.org/10.1016/j.isci.2019.04.025

iScience

CellPress

Article

Natrium Doping Pushes the Efficiency of Carbon-Based $CsPbI_3$ Perovskite Solar Cells to 10.7%

Sisi Xiang,[1] Weiping Li,[1] Ya Wei,[1] Jiaming Liu,[1] Huicong Liu,[1] Liqun Zhu,[1] Shihe Yang,[2,3,*] and Haining Chen[1,4,*]

SUMMARY

The $CsPbI_3$ inorganic perovskite is a potential candidate for fabricating long-term operational photovoltaic devices owing to its intrinsic superb thermal stability. However, the carbon-based $CsPbI_3$ perovskite solar cells (C-PSCs) without hole transport material (HTM) are currently disadvantaged by their relatively low power conversion efficiency resulting from the poor grain quality and mismatched energy band levels of the as-made $CsPbI_3$ films. Herein we demonstrate that by doping Na into the $CsPbI_3$ lattice, the grain quality is significantly improved with low defect density, and also, the energy band levels are better matched to the contact electrodes, affording a higher built-in potential. Consequently, the V_{oc} of the C-PSCs is drastically increased from 0.77 to 0.92 V, and the efficiency from 8.6% to 10.7%, a record value for the $CsPbI_3$ PSCs without HTM. Moreover, the non-encapsulated device showed virtually no performance degradation after 70 days of storage in air atmosphere.

INTRODUCTION

Organic-inorganic hybrid perovskite solar cells (PSCs) have attracted tremendous attention for their rapidly rising power conversion efficiency (PCE), currently reaching over 23%, achieved by solution-based techniques (Kojima et al., 2009; Lee et al., 2012; Mei et al., 2014; Yang et al., 2017). However, the organic ions in the organic-inorganic hybrid perovskites can easily escape from lattice under thermal stress, which restricts their long-term practical application (Wang et al., 2016; Park et al., 2016; Kim et al., 2016; Manser et al., 2016). In this regard, inorganic perovskites appear to be highly promising light absorbers owing to their good thermal stability (Duan et al., 2018; Yang et al., 2018). Among various inorganic perovskites, $CsPbI_3$ perovskite is the most suitable one because of its appropriate band gap (1.73 eV) for photovoltaic (PV) applications (Eperon et al., 2015; Frolova et al., 2016; Sanehira et al., 2017; Wang et al., 2018a, 2018c).

Other than the potential problems of perovskites as an active layer material in PSCs, the adoption of organic hole transport materials (HTMs) may also limit the stability of PSCs because they are commonly thermally unstable and susceptible to ion migration and metal electrode corrosion eventually causing device degradation (Swarnkar et al., 2016; Eperon et al., 2015; Luo et al., 2016; Liang et al., 2017b). To tackle this issue, proposal has been put forward to replace the organic HTM and the metal electrode with a carbon electrode, which for the past few years has proved to be an effective approach (Chen and Yang, 2017). Some works on carbon-based HTM-free PSCs (C-PSCs) have employed $CsPbI_3$ as a light absorber, and in our own work, a PCE of 9.5% has been achieved previously (Xiang et al., 2018). However, such a PCE is far lower than those achieved by the C-PSCs based on organic-inorganic hybrid perovskites. According to the previous works, the low PCE can be mainly attributable to the low obtainable open-circuit voltage (V_{oc}) (Ball et al., 2013; Han et al., 2015; Zhang et al., 2017; Liang et al., 2017a), i.e., below 0.8 V. The low V_{oc} should originate from the low grain quality of $CsPbI_3$ film or the mismatched energy band levels at charge collection interface (Ahmad et al., 2017; Eperon et al., 2015; Zhang et al., 2018; Chen et al., 2018; Sanehira et al., 2017).

Herein, we address the above issues by doping the $CsPbI_3$ inorganic perovskite at A site with Na element. It is found that the Na doping not only improved the morphology of $CsPbI_3$ film but also significantly enhanced the grain quality, thus reducing the defect density. Furthermore, the Na doping offers a good handle to adjust the energy band levels of $CsPbI_3$ film, raising the built-in potential and V_{oc}. As a result, C-PSCs based on the Na-doped $CsPbI_3$ film achieved a PCE as high as 10.7% with a V_{oc} of 0.92 V, which are considerably higher than those obtained by the C-PSCs based on pure $CsPbI_3$ film (PCE = 8.6%,

[1]School of Materials Science and Engineering, Beihang University, No. 37 Xueyuan Road, Haidian District, Beijing 100191, People's Republic of China

[2]Department of Chemistry, The Hong Kong University of Science and Technology, Clear Water Bay, Kowloon, Hong Kong, China

[3]Guangdong Key Lab of Nano-Micro Material Research, School of Chemical Biology and Biotechnology, Shenzhen Graduate School, Peking University, Shenzhen 518055, China

[4]Lead Contact

*Correspondence: chsyang@ust.hk (S.Y.), chenhaining@buaa.edu.cn (H.C.)

https://doi.org/10.1016/j.isci.2019.04.025

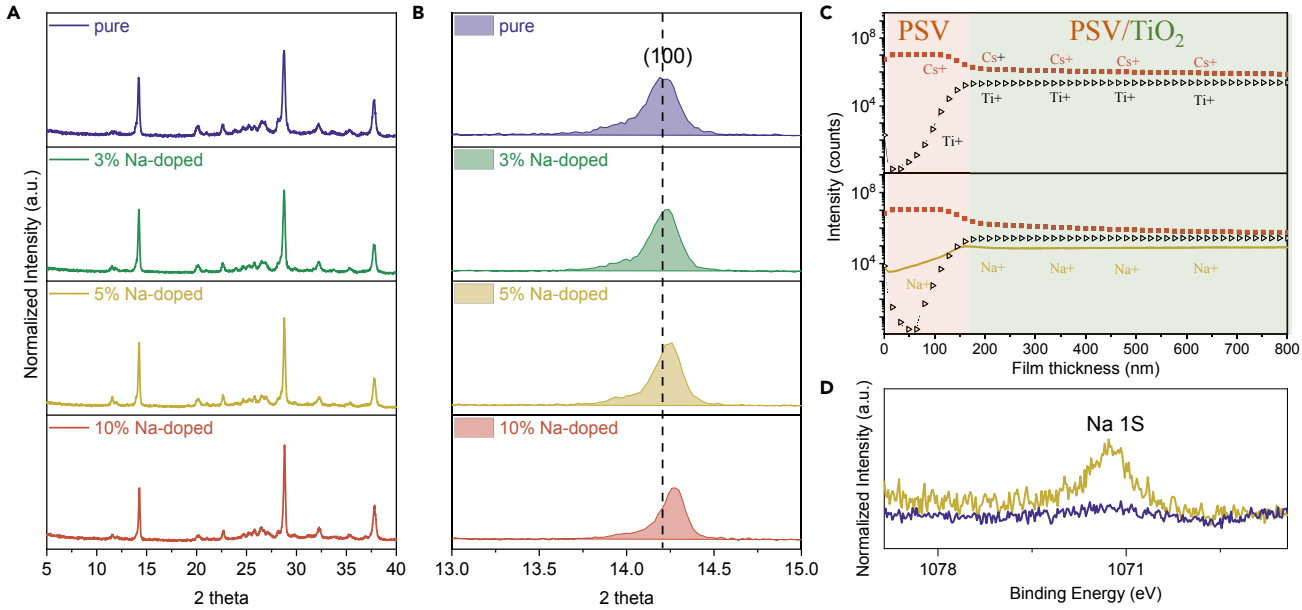

Figure 1. Composition Characterizations of $Cs_{1-x}Na_xPbI_3$ ($0 \leq x \leq 0.1$) Perovskite Films

(A) XRD patterns.

(B) Magnification of the (100) peak to show the peak shifts in the Na-doped film.

(C) Secondary ion mass spectroscopy depth profile for Cs, Pb, I, and Na elements of $CsPbI_3$ and $Cs_{0.95}Na_{0.05}PbI_3$ films.

(D) High-resolution XPS spectra of $CsPbI_3$ and $Cs_{0.95}Na_{0.05}PbI_3$ films.

V_{oc} = 0.77 V). Besides, the non-encapsulated C-PSCs based on the Na-doped $CsPbI_3$ film exhibit almost no PCE degradation after 70 days of storage in a dry air atmosphere.

The whole procedure of C-PSC fabrication, including $CsPbI_3$ deposition, was conducted in a dry air atmosphere (humidity~10%–20%). The $CsPbI_3$ films were deposited on TiO_2 mesoporous scaffolds via a one-step spin-coating method with the precursor solution containing ~1 M N,N-Dimethylformamide (DMF)·HI·PbI_2, (1-x) M CsI, and x M NaI, followed by heating at 200°C to obtain black $CsPbI_3$ perovskite films.

X-ray diffraction (XRD) patterns of the perovskite films with different Na doping concentrations are shown in Figure 1A. As depicted in Figures 1A and 1B, with Na doping content increasing, the (100) peak shifts to a higher 2θ, correlating to the lattice contraction. Therefore Na ions should have partially replaced Cs ions in the $CsPbI_3$ lattice because Na atoms (1.02Å) are significantly smaller than Cs atoms (1.67Å). Moreover, as depicted in Figure S1, the films after storage for 7 days show almost the same XRD patterns as the corresponding as-prepared films, suggesting high phase stability. Secondary ion mass spectroscopy was further employed to study the composition difference between $CsPbI_3$ and $Cs_{0.95}Na_{0.05}PbI_3$ films. The depth profiling in Figures 1C and S2 shows that Na ions have been doped into the $CsPbI_3$ film, which distribute throughout the whole film. As a side note, Na atom concentration in the capping layer is slightly lower than that in the mesoporous layer. This could be interpreted as follows. The tolerance factor of $CsPbI_3$ perovskite is small (t = 0.81), and it would be further lowered after the substitution of Cs with Na atoms, which would reduce the structural stability. To make the structure stable, Na atoms might thermodynamically tend to stay in the mesoporous TiO_2 scaffold, because the nanopores in the scaffold could confine grain dimensions to nanosize (Choi et al., 2013) and there may be lattice strain at the $CsPbI_3/TiO_2$ interface, which both would help to stabilize the perovskite structure. Similar phenomenon has been reported for organic-inorganic perovskites when the ions with a large size mismatch degree were used as dopants (Qiao et al., 2018). To identify the chemical states of $CsPbI_3$ and $Cs_{0.95}Na_{0.05}PbI_3$ films, X-ray photoelectron spectra (XPS) have also been recorded. The high-resolution XPS spectra for various elements (Na 1s, Cs 3d, Pb 4f and I 3d) are shown in Figures 1D and S3. Notably, a uniform shift in the peak positions of Cs 3d and Pb 4f to a lower binding energy is observed for $Cs_{0.95}Na_{0.05}PbI_3$ film, whereas the peak position of I 3d shifts to a higher binding energy. These shifts should be correlated to the Na doping because the smaller

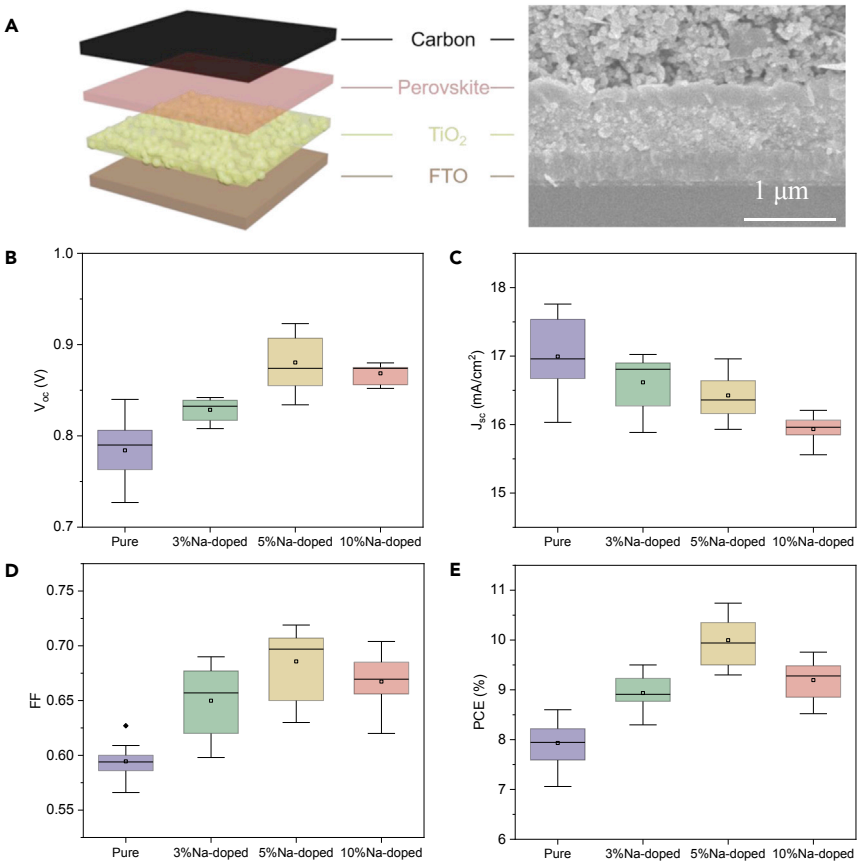

Figure 2. Device Structure and Photovoltaic Performance of $CsPbI_3$ and $Cs_{1-x}Na_xPbI_3$ ($0 \leq x \leq 0.1$) C-PSCs

(A) Scheme and cross-sectional SEM image of $CsPbI_3$ C-PSCs.

(B–E) Statistical box chart of (B) V_{oc}, (C) J_{sc}, (D) FF, and (E) PCE of $CsPbI_3$ and Na-doped $CsPbI_3$ C-PSCs.

Na atoms would cause the volume contraction of the BX_6 (B = Pb or Mn; X = I or Br) octahedral and hence lead to the changes in chemical bonding (Zou et al., 2017; Li et al., 2016).

To evaluate PV performance, paintable C-PSCs (as illustrated in Figure 2A) were fabricated by directly painting a commercial carbon paste on the $CsPbI_3$ and $Cs_{0.95}Na_{0.05}PbI_3$ films, followed by annealing at 120°C for 30 min (Chen et al., 2015, 2016). The cross-sectional scanning electron microscopic (SEM) image of the C-PSCs in Figure 2A indicates an intimate contact at the $CsPbI_3$/carbon interface.

The average PV parameters obtained from the $CsPbI_3$ and $Cs_{1-x}Na_xPbI_3$ ($0 \leq x \leq 0.1$) cells are shown in Figures 2B–2E. The average open-circuit voltage (V_{oc}) increases progressively with Na incorporation, from 0.78 $\pm$ 0.02 V for x = 0 to 0.88 $\pm$ 0.02 V for x = 0.05, and then slightly declines to 0.86 $\pm$ 0.01 V for x = 0.10. With Na doping concentration increasing, the short-circuit current density (J_{sc}) decreases gradually, from 17.0 $\pm$ 0.53 mA/cm^2 for x = 0 to 15.9 $\pm$ 0.1 mA/cm^2 for x = 0.10. Similar with V_{oc}, the fill factor (FF) also gradually increases as x increases from 0 to 0.05, and then reduces as x further increases to 0.10, with 5% Na (FF = 0.68 $\pm$ 0.02) outstanding among the others. As a result, the PCE increases from 7.9% $\pm$ 0.3% for the pristine $CsPbI_3$ device to 10.0% $\pm$ 0.4% for the $Cs_{0.95}Na_{0.05}PbI_3$ one. Interestingly, even for the perovskites containing 10% Na, the PV performance is still superior to the pure $CsPbI_3$, with an average PCE of 9.19% $\pm$ 0.3%.

The current density versus voltage (J-V) curves of the champion $CsPbI_3$ and $Cs_{0.95}Na_{0.05}PbI_3$ C-PSCs devices are presented in Figure 3A. The champion $CsPbI_3$ C-PSCs obtain a V_{oc} of 0.77 V, J_{sc} of 17.76 mA/cm^2, and FF of 0.627, which leads to a PCE of 8.6%, whereas the champion $Cs_{0.95}Na_{0.05}PbI_3$ device shows a V_{oc} of 0.92 V, J_{sc} of 16.5mA/cm^2, and FF of 0.703, which generates a PCE of 10.7%, a new record PCE for HTM-free

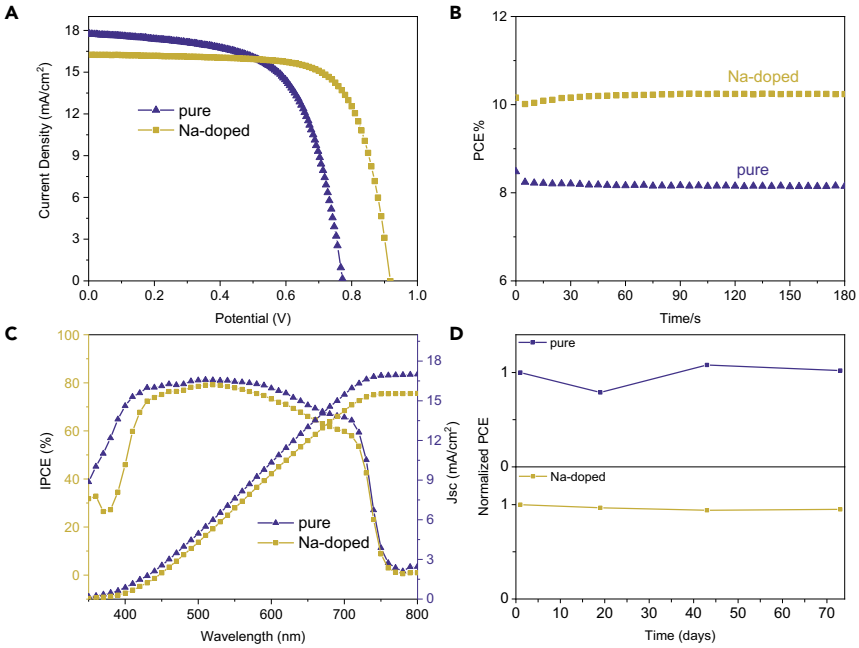

Figure 3. Champion Photovoltaic Performance of $CsPbI_3$ and $Cs_{0.95}Na_{0.05}PbI_3$ C-PSCs

(A–D) (A) J-V curves, (B) stabilized power output, (C) IPCE spectra and integrated J_{sc}, and (D) stability results of $CsPbI_3$ and $Cs_{0.95}Na_{0.05}PbI_3$ C-PSCs that were stored in dry air atmosphere (20°C –35°C and 10%–20% humidity). All devices used for the performance and stability testing were non-encapsulated.

$CsPbI_3$ PSCs (Liang et al., 2017a; Xiang et al., 2018). It can be clearly seen that the large increase in PCE mainly benefits from the obvious improved V_{oc} and FF, which would be further discussed below.

Figure 3B displays the plots of the PCEs that are obtained at the voltage close to the maximum power output point as a function of time, indicating that under constant illumination the steady-state PCEs of the $CsPbI_3$ and $Cs_{0.95}Na_{0.05}PbI_3$ C-PSCs are about 10.23% and 8.18%, respectively. In Figure S4, the J-V curves obtained from different scan directions show that both C-PSCs show similar hysteresis. The incident photon-to-electron conversion efficiency (IPCE) spectra (Figure 3C) are further taken for illustrating the J_{sc} decrease of the doped devices. Compared with $Cs_{0.95}Na_{0.05}PbI_3$ C-PSCs, $CsPbI_3$ C-PSCs show higher IPCE values in the whole wavelength, generating the integrated J_{sc} of 17.0 mA/cm^2 versus 15.55 mA/cm^2, which is well consistent with the J_{sc} extracted from the J-V curves. The cross-sectional SEM images in Figure S6A indicate that the film thickness of the two perovskite layers are almost the same (230 nm). Thus the lower absorption coefficient should be responsible for the decreased J_{sc} of Na-doped C-PSCs, as proved with the ultraviolet-visible (UV-vis) spectra in Figures 4C and S9.

The long-term stability of $CsPbI_3$ and $Cs_{0.95}Na_{0.05}PbI_3$ C-PSCs was also tested (Figure 3D) with the non-encapsulated devices stored in dry air atmosphere (20°C–35°C and 10%–20% humidity). Promisingly, both C-PSCs show excellent stability and almost no PCE degradation is detected after storage for more than 70 days. The photostability measurement of the devices under continuous one-sun illumination (100 mW/cm^{-2}) was also conducted in ambient atmosphere (20°C and 40% humidity). As shown in Figure S5, $Cs_{0.95}Na_{0.05}PbI_3$ device demonstrates a higher photostability than the $CsPbI_3$ one and 80% of the initial PCE has been retained after degradation for 24 h.

To get insights into the performance difference between the two C-PSCs, more characterizations on the perovskite films and C-PSCs were conducted. Top-view SEM images of $CsPbI_3$ and $Cs_{0.95}Na_{0.05}PbI_3$ films in Figures 4A and 4B show that after Na doping, the film surface becomes slightly smoother and the grain size becomes slightly larger, with the average size increasing from ~243 nm to around 288 nm (as shown in Figure S7). As further confirmed by atomic force microscopic images in Figure S6B, the roughness value (Ra) decreases from 19.9 to 18.3 nm after Na doping. However, such small improvement in film morphology could not well account for the PV performance difference.

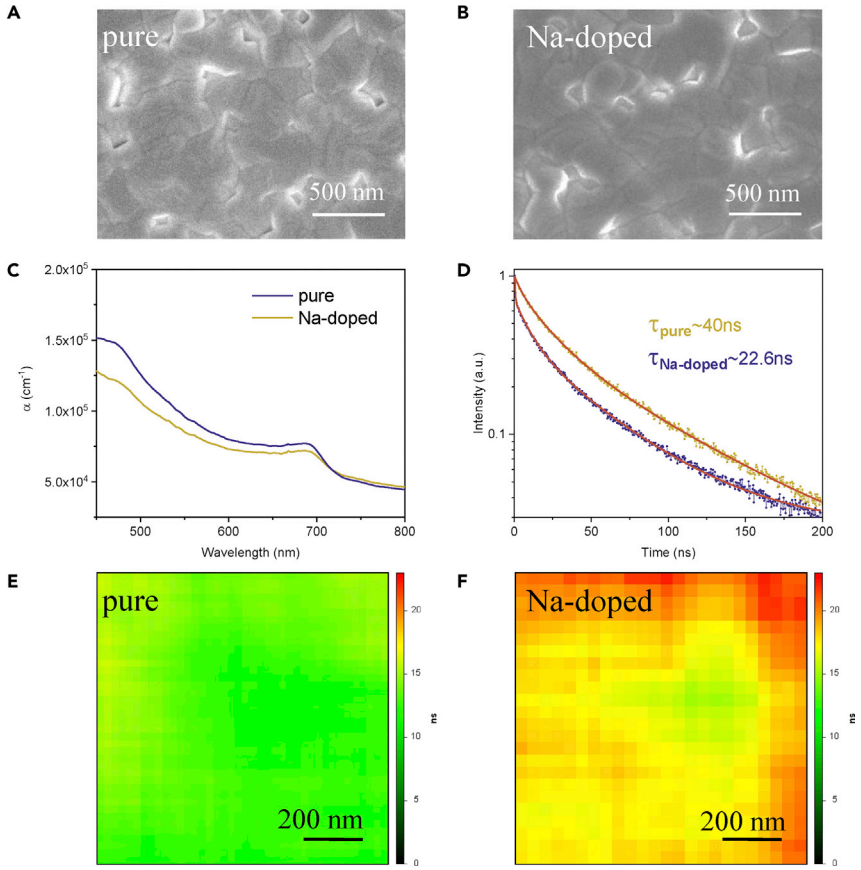

Figure 4. Morphology and Optoelectronic Properties of $CsPbI_3$ and $Cs_{0.95}Na_{0.05}PbI_3$ Films

(A and B) Top-view SEM images of (A) $CsPbI_3$ and (B) $Cs_{0.95}Na_{0.05}PbI_3$ films.

(C–F) (C) Absorption coefficient (α) versus wavelength curves and (D) TRPL of $CsPbI_3$ and $Cs_{0.95}Na_{0.05}PbI_3$ films. Fluorescence lifetime mapping images of (E) $CsPbI_3$ and (F) $Cs_{0.95}Na_{0.05}PbI_3$ films.

Absorption coefficient versus wavelength curves of $TiO_2/CsPbI_3$ and $TiO_2/Cs_{0.95}Na_{0.05}PbI_3$ thin films have been further measured. As shown in Figure 4C, the absorption coefficient decreases after Na doping, which well explains the decreased J_{sc} of the Na-doped devices. Steady-state photoluminescence (PL) and time-resolved PL (TRPL) spectra were further employed to evaluate the grain quality of $CsPbI_3$ and $Cs_{0.95}Na_{0.05}PbI_3$ films. As shown in Figure S8, the steady-state PL peaks of the two films appear at a very close wavelength, which is consistent with the UV-vis spectra in Figure S9. As shown in Figures S9C and S9D, the band gaps of $CsPbI_3$ and $Cs_{0.95}Na_{0.05}PbI_3$ are measured to be 1.67 and 1.68 eV, respectively. As clearly seen, the PL intensity of the $Cs_{0.95}Na_{0.05}PbI_3$ film is significantly higher than that of the $CsPbI_3$ film, suggesting a higher grain quality with less defects (Vorpahl et al., 2015; Tan et al., 2017; Pan et al., 2018). TRPL spectra of the bare perovskite films on glass substrate in Figure 4D show an obviously slower quenching rate after Na doping. After fitting, the average PL lifetime is calculated to be about 40 ns for the $Cs_{0.95}Na_{0.05}PbI_3$ film, almost two times longer than that of the $CsPbI_3$ film, well confirming the lower defect density induced by Na doping for suppressing charge recombination. To more vividly depict PL lifetime difference, the PL lifetimes throughout the perovskite films were also mapped. As shown in Figures 4E and 4F, the PL lifetime of the $CsPbI_3$ film is mainly around 10–15 ns, as highlighted by the light green color, whereas most of the area on the $Cs_{0.95}Na_{0.05}PbI_3$ film shows a PL lifetime of over 20 ns, as depicted by orange color. Therefore steady-state PL, TRPL, and PL lifetime mapping all confirm a higher grain quality with lower defect density after Na doping.

Mott-Schottky analyses of $CsPbI_3$ and $Cs_{0.95}Na_{0.05}PbI_3$ C-PSCs were carried out to get built-in potential (V_{bi}), which is related to the V_{oc} of C-PSCs (Laban and Etgar, 2013; Almora et al., 2016). As shown in Figure 5A, the V_{bi} can be obtained by using the intercept of the linear regime with the x axis of the

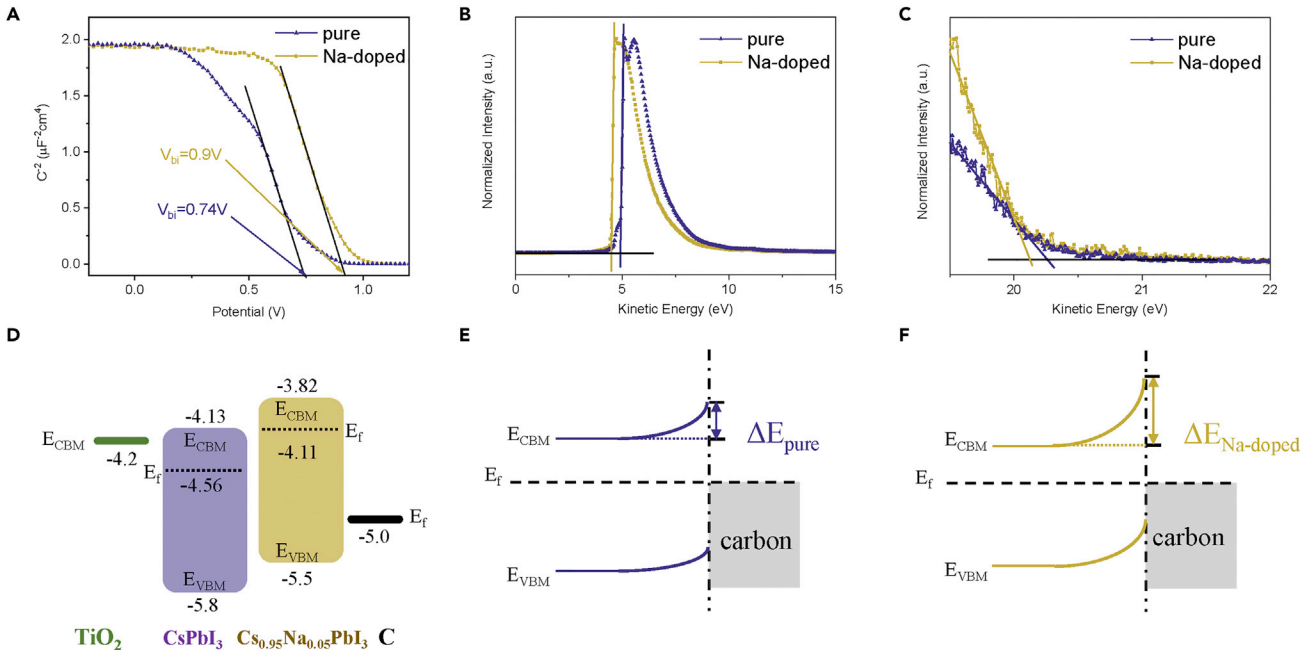

Figure 5. Junction Properties and Carrier Behaviors in C-PSCs

(A–C) (A) Mott-Schottky analysis at 10 kHz for $CsPbI_3$ and $Cs_{0.95}Na_{0.05}PbI_3$ C-PSCs. UV photoelectron spectroscopy of $CsPbI_3$ and $Cs_{0.95}Na_{0.05}PbI_3$ films: (B) cutoff region and (C) valence band edge region.

(D–F) (D) Energy level diagrams of $CsPbI_3$ and $Cs_{0.95}Na_{0.05}PbI_3$ C-PSCs, which were obtained from the UV photoemission spectroscopy results. Energy level diagram of the (E) $CsPbI_3$/carbon and (F) $Cs_{0.95}Na_{0.05}PbI_3$/carbon interfaces. E_{VBM} represents the energy level of valence band maximum, E_{CBM} represents the energy level of conduction band minimum, and E_f represents the Fermi level.

Mott-Schottky plot (Almora et al., 2016). The V_{bi} for the $CsPbI_3$ and $Cs_{0.95}Na_{0.05}PbI_3$ C-PSCs are about 0.74 V and 0.90 V, respectively. Such difference in V_{bi} is in good agreement with the V_{oc} values obtained from the J-V curves in Figure 2B. The larger V_{bi} would assist in more efficient charge separation and collection, which is favorable for achieving higher V_{oc} and FF (Wang et al., 2018b). Therefore the increase in V_{bi} should be an important cause for the performance improvement.

As well known, the difference in V_{bi} is usually reflected from the change in energy band levels (Wang et al., 2015). The energy band levels of $CsPbI_3$ and $Cs_{0.95}Na_{0.05}PbI_3$ films were characterized by the combination of UV photoelectron spectroscopy (Figures 5B and 5C) and UV-vis spectra (Figure S9). The final energy band levels of $CsPbI_3$ and $Cs_{0.95}Na_{0.05}PbI_3$ are depicted in Figure 5D. It can be indicated that both perovskite films are n-type semiconductors. Compared with $CsPbI_3$ film, all energy band levels of $Cs_{0.95}Na_{0.05}PbI_3$ film are obviously lifted, especially for E_f. The higher E_{CBM} may be favorable for electron injection from $Cs_{0.95}Na_{0.05}PbI_3$ to TiO_2. The lifting of the E_f would induce a larger upward band bending at the $Cs_{0.95}Na_{0.05}PbI_3$/carbon interface as depicted in Figures 5E and 5F, which would promote hole transfer. The obtained V_{bi} from the Mott-Schottky analysis may predominantly form at perovskite/carbon interface because the potential drop at the n-n junction of TiO_2/perovskite interface should be negligible (Jiang et al., 2015; Guerrero et al., 2014).

According to intensity-modulated photocurrent/photovoltage spectroscopy results, the relationship of light intensity (I_0) with electron diffusion coefficients (D_n) and electron lifetime (τ_n) could be obtained, as shown in Figure S10. Based on the equation $L_n=(D_n\tau_n)^{1/2}$, diffusion length (L_n) could be calculated (Zhu et al., 2007; Zhao and Zhu, 2013). As depicted in Figure S10C, the L_n of $Cs_{0.95}Na_{0.05}PbI_3$ C-PSCs is obviously larger than that of $CsPbI_3$ C-PSCs, which further confirms the lower charge recombination loss and more efficient charge collection.

In conclusion, we have significantly increased the V_{oc} and PCE of $CsPbI_3$ C-PSCs by doping Na into the $CsPbI_3$ lattice. The resulting morphology shows a slight difference between $CsPbI_3$ and $Cs_{0.95}Na_{0.05}PbI_3$ films, but the grain quality was significantly improved with a lower defect density for the doped sample.

Spectroscopic measurements showed that all energy band levels (E_{VBM}, E_{CBM}, and E_f) were lifted up after Na doping, which afforded a better match to the contact electrode and hence supported a larger V_{bi} for obtaining a higher V_{oc} (0.92 V) for C-PSCs. As a result, the $Cs_{0.95}Na_{0.05}PbI_3$ C-PSCs achieved a PCE as high as 10.7%, which is a new record value for the α-$CsPbI_3$ PSCs without HTM. More promisingly, the non-encapsulated $Cs_{0.95}Na_{0.05}PbI_3$ C-PSCs exhibited almost no performance degradation after 70-day storage in a dry air atmosphere. Therefore Na doping is an effective way to fabricate $CsPbI_3$ C-PSCs with high performance and high stability.

Limitations of the Study

Organic-inorganic hybrid PSCs have attracted great interest because of their rapidly rising PCE. However, the volatility of the organic cations in these materials restricts long-term practical application. The $CsPbI_3$ inorganic perovskite with intrinsic superb thermal stability is a potential candidate to fabricate prolonged stable operational PV devices. However, the efficiency of carbon-based PSCs (C-PSCs) without HTM, the most promising commercial PSCs, is relatively low due to the poor crystalline quality and mismatched energy band levels of $CsPbI_3$. Herein, by doping Na into the $CsPbI_3$ lattice, the PCE of C-PSCs is largely improved especially the open circuit potential. The important achievements are as follows:

(1) The Na doping not only improves the morphology of $CsPbI_3$ film but also significantly enhances crystalline quality to reduced defect density.

(2) All energy band levels of $CsPbI_3$ are lifted up to match contact electrodes after Na doping, which helps to support a much higher built-in potential for obtaining an increased V_{oc} from 0.77 to 0.92 V.

(3) Na-doped C-PSCs achieve an efficiency of 10.7%, a new record value of the $CsPbI_3$ PSCs without HTM.

(4) The non-encapsulated Na-doped C-PSCs exhibit almost no performance degradation after 70 days of storage in air atmosphere.

METHODS

All methods can be found in the accompanying Transparent Methods supplemental file.

SUPPLEMENTAL INFORMATION

Supplemental Information can be found online at https://doi.org/10.1016/j.isci.2019.04.025.

ACKNOWLEDGMENTS

This work is financially supported by the Young Talent of "Zhuoyue" Program of Beihang University, the National Natural Science Foundation of China (21875013 and 21603010), and the Beijing Natural Science Foundation (No. 2182031). The authors would like to thank Senior Engineer Yan Guan in Peking University Analytical Instrumentation Center for the fluorescence lifetime mapping image supports. Shenzhen Peacock Plan (KQTD2016053015544057), the HK-RGC General Research Funds (GRF Nos. 16312216) and the HK Innovation and Technology Fund (GHP/079/17SZ).

AUTHOR CONTRIBUTIONS

H.C. proposed the research and directed the study. S.X. prepared and characterized the perovskite films. Y.W. and J.L. helped with the device fabrication and characterization. W.L., H.L., and L.Z. helped analyzed the data. S.X., H.C., and S.Y. prepared the manuscript.

DECLARATION OF INTERESTS

The authors declare no competing interests.

Received: December 10, 2018
Revised: March 28, 2019
Accepted: April 19, 2019
Published: May 31, 2019

REFERENCES

Ahmad, W., Khan, J., Niu, G., and Tang, J. (2017). Inorganic CsPbI3 perovskite-based solar cells: a choice for a tandem device. Solar RRL *1*, 1700048.

Almora, O., Aranda, C., Mas-Marzá, E., and Garcia-Belmonte, G. (2016). On Mott-Schottky analysis interpretation of capacitance measurements in organometal perovskite solar cells. Appl. Phys. Lett. *109*, 173903.

Ball, J.M., Lee, M.M., Hey, A., and Snaith, H.J. (2013). Low-temperature processed meso-superstructured to thin-film perovskite solar cells. Energy Environ. Sci. *6*, 1739–1743.

Chen, H., Wei, Z., He, H., Zheng, X., Wong, K.S., and Yang, S. (2016). Solvent engineering boosts the efficiency of paintable carbon-based perovskite solar cells to beyond 14%. Adv. Energy Mater. *6*, 1502087.

Chen, H., Wei, Z., Zheng, X., and Yang, S. (2015). A scalable electrodeposition route to the low-cost, versatile and controllable fabrication of perovskite solar cells. Nano Energy *15*, 216–226.

Chen, H., Xiang, S., Li, W., Liu, H., Zhu, L., and Yang, S. (2018). Inorganic perovskite solar cells: a rapidly growing field. Solar RRL *2*, 1700188.

Chen, H., and Yang, S. (2017). Carbon-based perovskite solar cells without hole transport materials: the front runner to the market? Adv. Mater. *29*, 1603994.

Choi, J.J., Yang, X., Norman, Z.M., Billinge, S.J., and Owen, J.S. (2013). Structure of methylammonium lead iodide within mesoporous titanium dioxide: active material in high-performance perovskite solar cells. Nano Lett. *14*, 127–133.

Duan, J., Zhao, Y., He, B., and Tang, Q. (2018). High-purity inorganic perovskite films for solar cells with 9.72% efficiency. Angew. Chem. Int. Ed. *130*, 3849–3853.

Eperon, G.E., Paterno, G.M., Sutton, R.J., Zampetti, A., Haghighirad, A.A., Cacialli, F., and Snaith, H.J. (2015). Inorganic caesium lead iodide perovskite solar cells. J. Mater. Chem. A *3*, 19688–19695.

Frolova, L.A., Anokhin, D.V., Piryazev, A.A., Luchkin, S.Y., Dremova, N.N., Stevenson, K.J., and Troshin, P.A. (2016). Highly efficient all-inorganic planar heterojunction perovskite solar cells produced by thermal coevaporation of CsI and PbI2. J. Phys. Chem. Lett. *8*, 67–72.

Guerrero, A., Juarez-Perez, E.J., Bisquert, J., Mora-Sero, I., and Garcia-Belmonte, G. (2014). Electrical field profile and doping in planar lead halide perovskite solar cells. Appl. Phys. Lett. *105*, 133902.

Han, G.S., Chung, H.S., Kim, B.J., Kim, D.H., Lee, J.W., Swain, B.S., Mahmood, K., Yoo, J.S., Park, N.-G., and Lee, J.H. (2015). Retarding charge recombination in perovskite solar cells using ultrathin MgO-coated TiO 2 nanoparticulate films. J. Mater. Chem. A *3*, 9160–9164.

Jiang, C.-S., Yang, M., Zhou, Y., To, B., Nanayakkara, S.U., Luther, J.M., Zhou, W., Berry, J.J., van de Lagemaat, J., and Padture, N.P. (2015). Carrier separation and transport in perovskite solar cells studied by nanometre-scale profiling of electrical potential. Nat. Commun. *6*, 8397.

Kim, H.S., Seo, J.Y., and Park, N.G. (2016). Material and device stability in perovskite solar cells. ChemSusChem *9*, 2528–2540.

Kojima, A., Teshima, K., Shirai, Y., and Miyasaka, T. (2009). Organometal halide perovskites as visible-light sensitizers for photovoltaic cells. J. Am. Chem. Soc. *131*, 6050–6051.

Laban, W.A., and Etgar, L. (2013). Depleted hole conductor-free lead halide iodide heterojunction solar cells. Energy Environ. Sci. *6*, 3249–3253.

Lee, M.M., Teuscher, J., Miyasaka, T., Murakami, T.N., and Snaith, H.J. (2012). Efficient hybrid solar cells based on meso-superstructured organometal halide perovskites. Science *338*, 643–647.

Li, Z., Yang, M., Park, J.-S., Wei, S.-H., Berry, J.J., and Zhu, K. (2016). Stabilizing perovskite structures by tuning tolerance factor: formation of formamidinium and cesium lead iodide solid-state alloys. Chem. Mater. *28*, 284–292.

Liang, J., Wang, C., Zhao, P., Lu, Z., Ma, Y., Xu, Z., Wang, Y., Zhu, H., Hu, Y., and Zhu, G. (2017a). Solution synthesis and phase control of inorganic perovskites for high-performance optoelectronic devices. Nanoscale *9*, 11841–11845.

Liang, J., Zhao, P., Wang, C., Wang, Y., Hu, Y., Zhu, G., Ma, L., Liu, J., and Jin, Z. (2017b). CsPb0. 9Sn0. 1IBr2 based all-inorganic perovskite solar cells with exceptional efficiency and stability. J. Am. Chem. Soc. *139*, 14009–14012.

Luo, P., Xia, W., Zhou, S., Sun, L., Cheng, J., Xu, C., and Lu, Y. (2016). Solvent engineering for ambient-air-processed, phase-stable CsPbI3 in perovskite solar cells. J. Phys. Chem. Lett. *7*, 3603–3608.

Manser, J.S., Saidaminov, M.I., Christians, J.A., Bakr, O.M., and Kamat, P.V. (2016). Making and breaking of lead halide perovskites. Acc. Chem. Res. *49*, 330–338.

Mei, A., Li, X., Liu, L., Ku, Z., Liu, T., Rong, Y., Xu, M., Hu, M., Chen, J., and Yang, Y. (2014). A hole-conductor–free, fully printable mesoscopic perovskite solar cell with high stability. Science *345*, 295–298.

Pan, J., Shang, Y., Yin, J., de Bastiani, M., Peng, W., Dursun, I., Sinatra, L., el-Zohry, A.M., Hedhili, M.N., and Emwas, A.-H. (2018). Bidentate ligand-passivated CsPbI3 perovskite nanocrystals for stable near-unity photoluminescence quantum yield and efficient red light-emitting diodes. J. Am. Chem. Soc. *140*, 562–565.

Park, N.-G., Grätzel, M., Miyasaka, T., Zhu, K., and Emery, K. (2016). Towards stable and commercially available perovskite solar cells. Nat. Energy *1*, 16152.

Qiao, H.W., Yang, S., Wang, Y., Chen, X., Wen, T.Y., Tang, L.J., Cheng, Q., Hou, Y., Zhao, H., and Yang, H.G. (2018). A gradient heterostructure based on tolerance factor in high-performance perovskite solar cells with 0.84 fill factor. Adv. Mater. *31*, 1804217.

Sanehira, E.M., Marshall, A.R., Christians, J.A., Harvey, S.P., Ciesielski, P.N., Wheeler, L.M., Schulz, P., Lin, L.Y., Beard, M.C., and Luther, J.M. (2017). Enhanced mobility CsPbI3 quantum dot arrays for record-efficiency, high-voltage photovoltaic cells. Sci. Adv. *3*, eaao4204.

Swarnkar, A., Marshall, A.R., Sanehira, E.M., Chernomordik, B.D., Moore, D.T., Christians, J.A., Chakrabarti, T., and Luther, J.M. (2016). Quantum dot–induced phase stabilization of α-CsPbI3 perovskite for high-efficiency photovoltaics. Science *354*, 92–95.

Tan, H., Jain, A., Voznyy, O., Lan, X., de Arquer, F.P.G., Fan, J.Z., Quintero-Bermudez, R., Yuan, M., Zhang, B., and Zhao, Y. (2017). Efficient and stable solution-processed planar perovskite solar cells via contact passivation. Science *355*, 722–726.

Vorpahl, S.M., Stranks, S.D., Nagaoka, H., Eperon, G.E., Ziffer, M.E., Snaith, H.J., and Ginger, D.S. (2015). Impact of microstructure on local carrier lifetime in perovskite solar cells. Science *348*, 683–686.

Wang, C., Liu, X., Wang, C., Xiao, Z., Bi, C., Shao, Y., Huang, J., and Gao, Y. (2015). Surface analytical investigation on organometal triiodide perovskite. J. Vac. Sci. Tech. B *33*, 032401.

Wang, D., Wright, M., Elumalai, N.K., and Uddin, A. (2016). Stability of perovskite solar cells. Solar Energy Mater. Sol. Cells *147*, 255–275.

Wang, P., Zhang, X., Zhou, Y., Jiang, Q., Ye, Q., Chu, Z., Li, X., Yang, X., Yin, Z., and You, J. (2018a). Solvent-controlled growth of inorganic perovskite films in dry environment for efficient and stable solar cells. Nat. Commun. *9*, 2225.

Wang, S., Sakurai, T., Wen, W., and Qi, Y. (2018b). Energy level alignment at interfaces in metal halide perovskite solar cells. Adv. Mater. Interfaces *5*, 1800260.

Wang, Y., Zhang, T., Kan, M., and Zhao, Y. (2018c). Bifunctional stabilization of all-inorganic α-CsPbI3 perovskite for 17% efficiency photovoltaics. J. Am. Chem. Soc. *140*, 12345–12348.

Xiang, S., Fu, Z., Li, W., Wei, Y., Liu, J., Liu, H., Zhu, L., Zhang, R., and Chen, H. (2018). Highly air-stable carbon-based α-CsPbI3 perovskite solar cells with a broadened optical spectrum. ACS Energy Lett. *3*, 1824–1831.

Yang, F., Hirotani, D., Kapil, G., Kamarudin, M.A., Ng, C.H., Zhang, Y., Shen, Q., and Hayase, S. (2018). All-inorganic CsPb1-xGexI2Br perovskite with enhanced phase stability and photovoltaic performance. Angew. Chem. Int. Ed. *57*, 12745–12749.

Yang, W.S., Park, B.-W., Jung, E.H., Jeon, N.J., Kim, Y.C., Lee, D.U., Shin, S.S., Seo, J., Kim, E.K., and Noh, J.H. (2017). Iodide management in formamidinium-lead-halide–based perovskite layers for efficient solar cells. Science *356*, 1376–1379.

Zhang, T., Dar, M.I., Li, G., Xu, F., Guo, N., Grätzel, M., and Zhao, Y. (2017). Bication lead iodide 2D perovskite component to stabilize inorganic α-CsPbI3 perovskite phase for high-efficiency solar cells. Sci. Adv. *3*, e1700841.

Zhang, X., Zhang, J., Phuyal, D., Du, J., Tian, L., Öberg, V.A., Johansson, M.B., Cappel, U.B., Karis, O., and Liu, J. (2018). Inorganic CsPbI3 perovskite coating on PbS quantum dot for highly efficient and stable infrared light converting solar cells. Adv. Energy Mater. *8*, 1702049.

Zhao, Y., and Zhu, K. (2013). Charge transport and recombination in perovskite (CH3NH3) PbI3 sensitized TiO2 solar cells. J. Phys. Chem. Lett. *4*, 2880–2884.

Zhu, K., Neale, N.R., Miedaner, A., and Frank, A.J. (2007). Enhanced charge-collection efficiencies and light scattering in dye-sensitized solar cells using oriented TiO2 nanotubes arrays. Nano Lett. *7*, 69–74.

Zou, S., Liu, Y., Li, J., Liu, C., Feng, R., Jiang, F., Li, Y., Song, J., Zeng, H., and Hong, M. (2017). Stabilizing cesium lead halide perovskite lattice through Mn (II) substitution for air-stable light-emitting diodes. J. Am. Chem. Soc. *139*, 11443–11450.

ISCI, Volume *15*

Supplemental Information

Natrium Doping Pushes the Efficiency of Carbon-Based $CsPbI_3$ Perovskite Solar Cells to 10.7%

Sisi Xiang, Weiping Li, Ya Wei, Jiaming Liu, Huicong Liu, Liqun Zhu, Shihe Yang, and Haining Chen

Transparent Methods

Preparation of TiO_2 mesoporous scaffolds. Firstly, TiO_2 blocking layer was spin-coated on cleaned FTO glass at 2000 rpm for 20 s using 0.15 M titanium diisopropoxide bis(acetylacetonate) in 1-butanol solution, followed by heating at 125 °C for 5 min. Then, TiO_2 films was deposited by spin coating at 5000 rpm for 30 s using a commercial TiO_2 paste (Dyesol 30 NRD, Dyesol) diluted in ethanol with a ratio of 1:2.5. After drying at 100 °C for 5 min, the TiO_2 films were gradually heated to 550 °C, baked at this temperature for 30 min and cooled to room temperature.

Deposition of $CsPbI_3$ and $Cs_{1-x}Na_xPbI_3$ films. DMF·HI·PbI_2 powder was prepared as introduced in our previous work[6]. mixing 5 g PbI_2 and 4 ml HI in DMF and stirring overnight to ensure complete conversion. Light yellow DMF·HI·PbI_2 precipitates were obtained by pouring abundant ethanol into the above solution, followed by washing the precursor in ethanol for several times. The precipitates was filtered and dried in a vacuum oven at 60 °C for 2 h. $CsPbI_3$ films were deposited by one-step deposition method. The $CsPbI_3$ precursor solution was prepared by dissolving 1 M DMF·HI·PbI_2 and 1M CsI in DMF solvent at room temperature. The solution was spin-coated on the substrates that had been preheated to 70 °C at 2000 rpm for 20 s. Then, the samples were annealed at 200 °C for around 5 min to get $CsPbI_3$ films. For the $Cs_{1-x}Na_xPbI_3$ films, the whole procedure was similar except replacing xM CsI with NaI in the precursor solution.

Deposition of carbon electrode. A commercial carbon paste purchased from Guangzhou Seaside Technology Co., Ltd was used as carbon paint for carbon electrode. The carbon extraction layer was simply deposited by printing the carbon paint on $CsPbI_3$ films at room temperature, followed by heating at 120 °C for 30 min.

Films characterizations. X-ray diffraction (XRD) patterns were recorded on a Philips PW-1830 X-ray diffractometer with Cu Kα radiation (K = 0.15418 nm). TOF-SIM was used to detect distribution of different elements, collected in the positive ion detection mode employing 30 keV Bi+ primary beam with a diameter of 100 um and recorded on TOF.SIMS 5-100. The beam was at an angle of 45º with respect to the sample surface normal. Morphology was evaluated on a JEOL 6700F or 7100F SEM at an accelerating voltage of 5 kV. UV-vis absorption spectra were recorded on a Perkin-Elmer UV-vis spectrophotometer (model Lambda 20). Steady state PL spectra were measured on a Jobin Yvon (Laboratory RAM HR800) confocal micro-Raman spectrometer. Time resolved PL measurement was carried out on an ultrafast lifetime Spectrofluorometer (Delta flex) and a 475 nm ultrafast laser was used as the excitation light source. Fluorescence lifetime image were recorded on a laser scanning confocal microscope (A1R-si). Chemical states of film surface were evaluated by an X-ray photoemission spectroscopy (XPS, ESCALab250Xi). The energy positions were recorded on an ultraviolet photoelectron spectroscopy (UPS, ESCALab250Xi).

Photovoltaic characterizations. The solar light simulator (Newport Oriel Sol3A, model number 94063A, AM 1.5 global filter) was calibrated to 1 sun (100 mW/cm^2) using an Oriel reference solar cell (monocrystalline silicon) and meter. The active cell area was all fixed at about 6.25 mm^2 using a metal mask. Each ten cells were used to collect the relevant cell parameters of different doping amount in Figure 2(b)-(e). J–V curves and intensity modulated photocurrent/photovoltage spectroscopy (IMPS/IMVS) and open-circuit voltage decay (OCVD) measurement were recorded

on a ZENNIUM pro electrochemical workstation (ZAHNER-Elektrik GmbH & Co., KG, Germany). The wavelength of the irradiation light for IMPVS and OCVD measurement is 417 nm. IPCE spectra were recorded using IPCE kit (E0201, Institute of Physics, Chinese Academy of Sciences) in AC mode.

Stability evaluation. The device stability was studied by storing the device under room temperature (20-30 °C) in air atmosphere with a humidity lower than 30 %. J-V curves were measured periodically in ambient air (about 30-80 % humidity) to get the photovoltaic parameters. The photostability was tested under continuous one-sun illumination (100 mW/cm^{-2}) at RT and 65 °C in ambient atmosphere without encapsulation (humidity~40%).

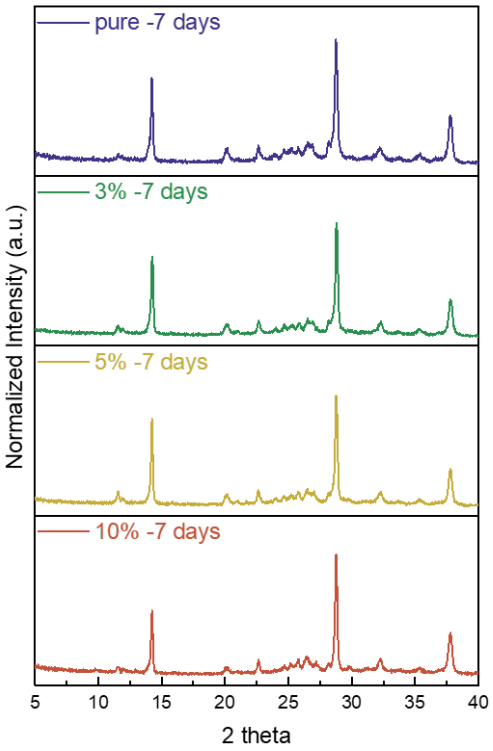

Figure S1. XRD patterns of the $CsPbI_3$ perovskite films with different Na doping concentrations after 7 days storage in air atmosphere (20-35 °C and 10-20% humidity). Related to Figure 1(a).

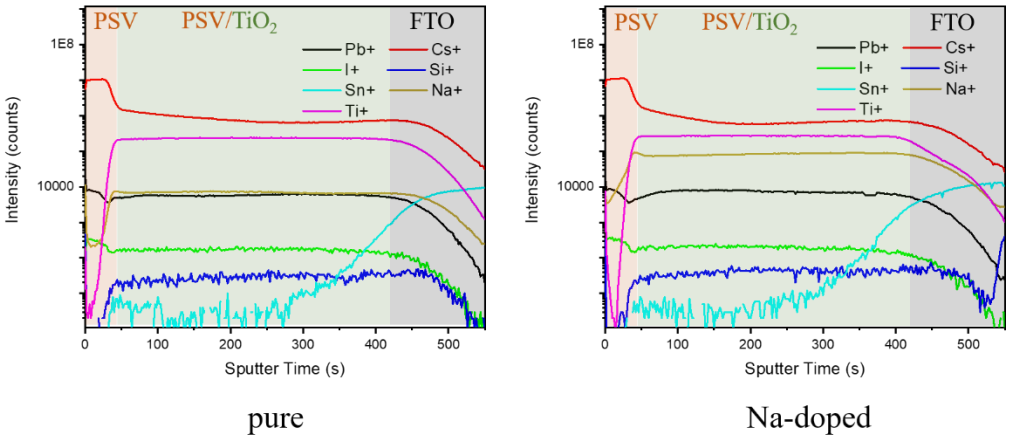

Figure S2. SIMS depth profile for Cs, Pb, I, Na, Sn, Si and Ti elements in $CsPbI_3$ and $Cs_{0.95}Na_{0.05}PbI_3$ films. Related to Figure 1(c).

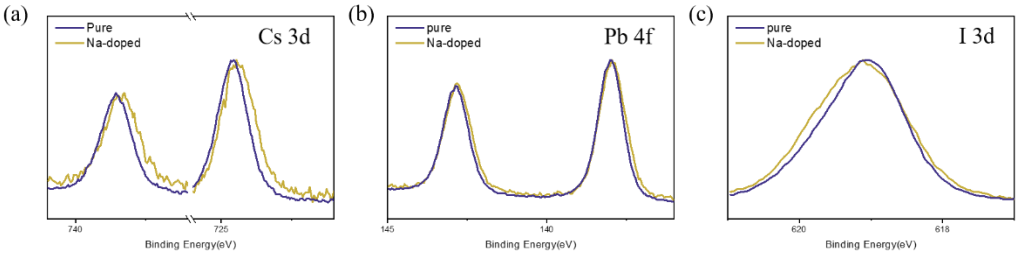

Figure S3. Comparison of high-resolution XPS spectra of the $CsPbI_3$ and $Cs_{0.95}Na_{0.05}PbI_3$ films: (a) Cs 3d. (b) Pb 4f. (c) I 3d. Related to Figure 1(d).

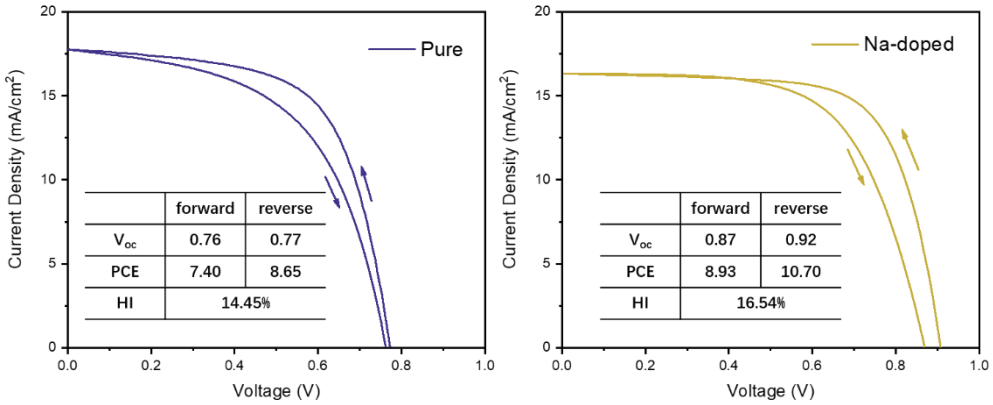

Figure S4. J-V curves obtained from different scan directions of $CsPbI_3$ and $Cs_{0.95}Na_{0.05}PbI_3$ C-PSCs. Insets are the cell parameters obtained from different scan directions. Related to Figure 3.

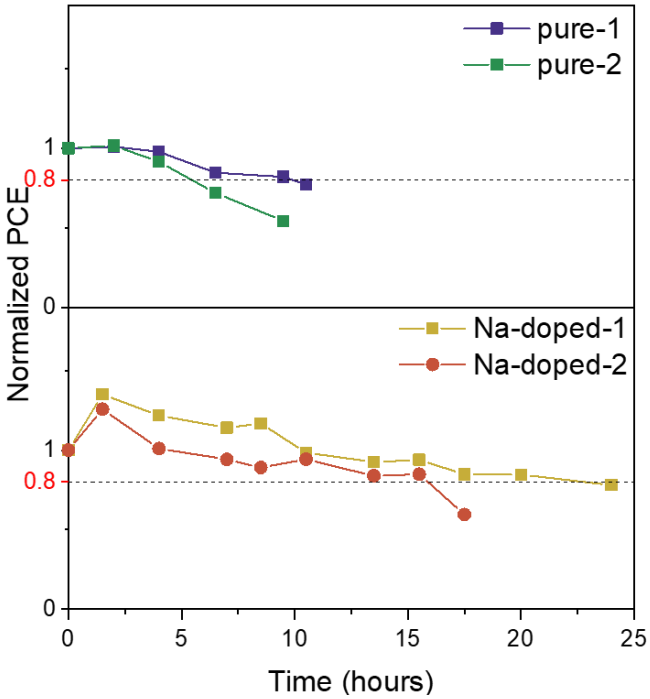

Figure S5. Photostability measurement of the devices under continuous one-sun illumination (100 mW/cm^{-2}) in ambient atmosphere without encapsulation (room temperature (about 20 ℃) and humidity~40%). Related to Figure 3.

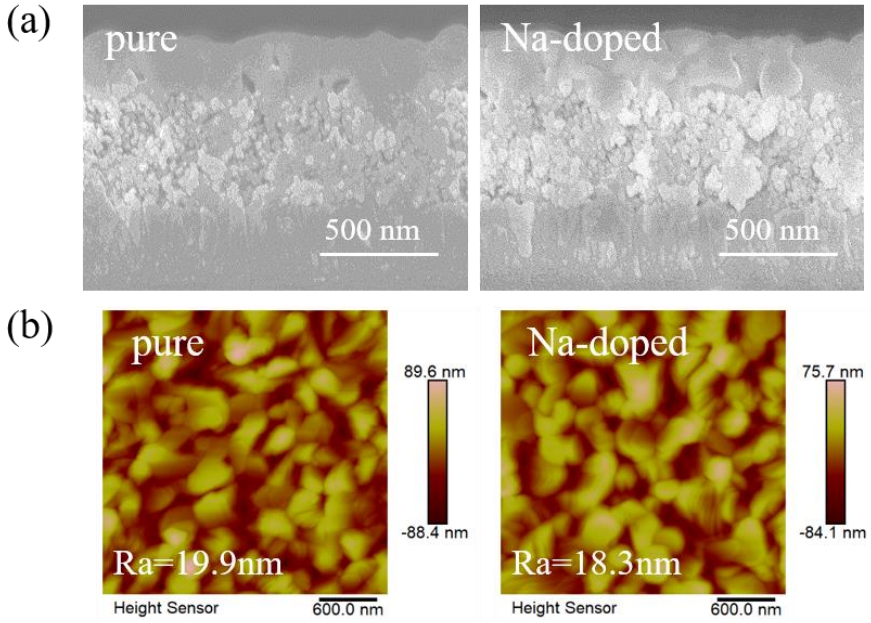

Figure S6. Morphology of $CsPbI_3$ and $Cs_{0.95}Na_{0.05}PbI_3$ films. (a) Cross-sectional SEM images (b) AFM images. Related to Figure 3 and 4.

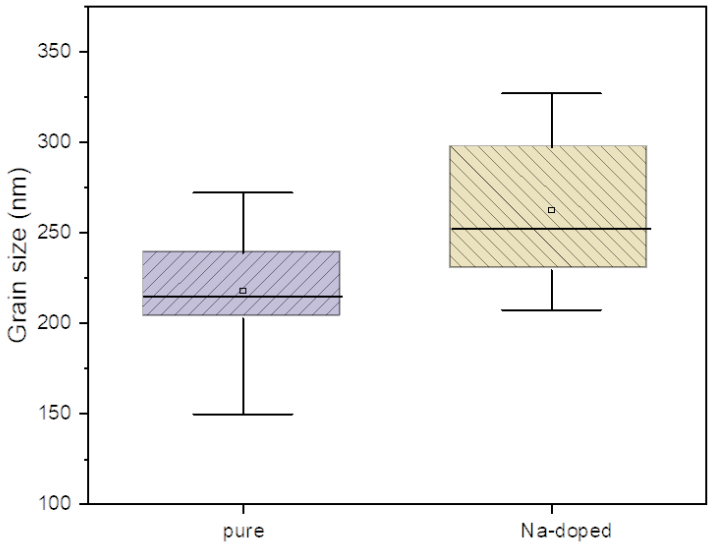

Figure S7. Grain size distribution of $CsPbI_3$ and $Cs_{0.95}Na_{0.05}PbI_3$ films. Related to Figure 4.

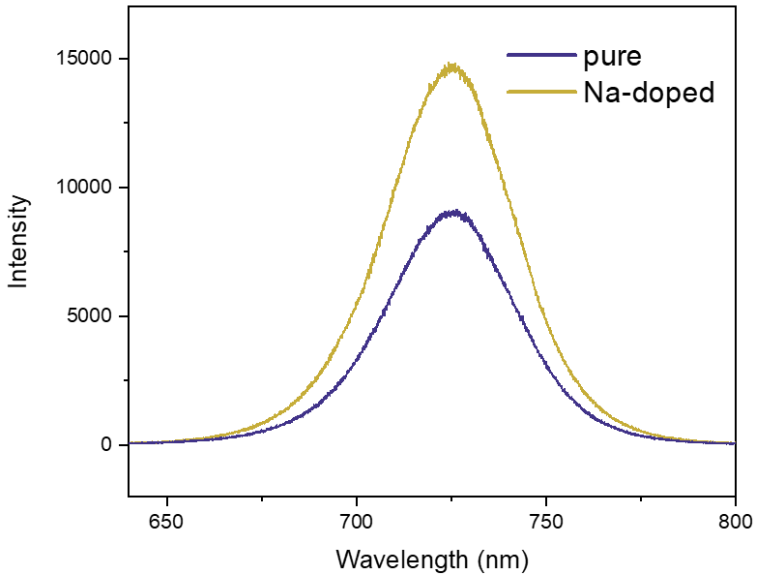

Figure S8. Steady-state PL of $CsPbI_3$ and $Cs_{0.95}Na_{0.05}PbI_3$ films. Related to Figure 4.

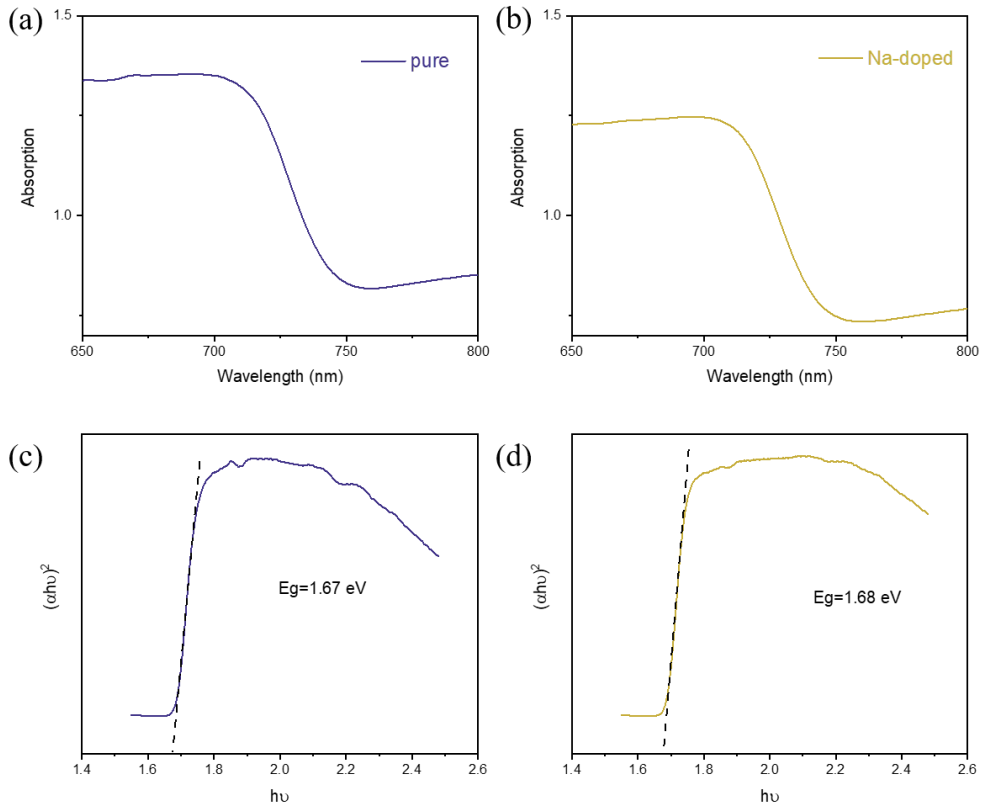

Figure S9. UV-vis spectra of (a) $CsPbI_3$ and (b) $Cs_{0.95}Na_{0.05}PbI_3$ films. $(\alpha h\nu)^2$ vs hν curves of (c) $CsPbI_3$ and (d) $Cs_{0.95}Na_{0.05}PbI_3$ films. Related to Figure 4.

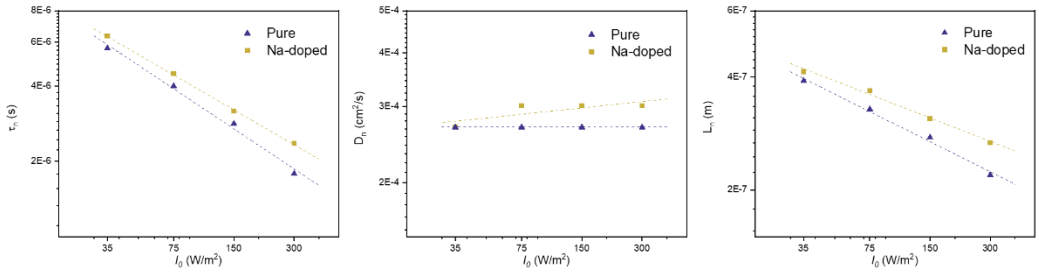

Figure S10. (a) Electron lifetime (τ_n), (b) electron diffusion coefficients (D_n) and (c) diffusion length (L_n) as a function of light density (I_0) for $CsPbI_3$ and $Cs_{0.95}Na_{0.05}PbI_3$ C-PSCs. Related to Figure 5.